Geophysical Research Letters

RESEARCH LETTER
10.1029/2024GL109433

Depth Dependent Deformation and Anisotropy of Pyrolite in the Earth's Lower Mantle

Jeffrey P. Gay[1], Estelle E. Ledoux[1], Matthias Krug[2], Julien Chantel[1], Anna Pakhomova[3], Carmen Sanchez-Valle[2], Sergio Speziale[4], and Sébastien Merkel[1]

[1]Univ. Lille, CNRS, INRAE, Centrale Lille, UMR 8207—UMET—Unité Matériaux et Transformations, Lille, France, [2]Institute of Mineralogy, University of Münster, Münster, Germany, [3]Deutsches Elektronen-Synchrotron (DESY), Hamburg, Germany, [4]GFZ German Research Centre for Geoscience, Postsdam, Germany

Key Points:

- Three microstructure/anisotopy regimes in bridgmanite in the Earth's lower mantle: transformation, low-P deformation, high-P deformation
- Effect of pressure on the active slip systems of bridgmanite with a shift at approximately 50 GPa or 1,300 km depth in the Earth's mantle
- Up to 2% shear wave splitting predicted at all depth with changes in fast polarization direction for each microstructural regime

Supporting Information:

Supporting Information may be found in the online version of this article.

Correspondence to:

J. P. Gay and S. Merkel,
jgay@princeton.edu;
sebastien.merkel@univ-lille.fr

Citation:

Gay, J. P., Ledoux, E. E., Krug, M., Chantel, J., Pakhomova, A., Sanchez-Valle, C., et al. (2024). Depth dependent deformation and anisotropy of pyrolite in the Earth's lower mantle. *Geophysical Research Letters*, *51*, e2024GL109433. https://doi.org/10.1029/2024GL109433

Received 22 MAR 2024
Accepted 26 APR 2024

Author Contributions:

Conceptualization: Carmen Sanchez-Valle, Sergio Speziale, Sébastien Merkel
Formal analysis: Jeffrey P. Gay, Estelle E. Ledoux, Matthias Krug, Sébastien Merkel
Funding acquisition: Carmen Sanchez-Valle, Sergio Speziale, Sébastien Merkel
Investigation: Jeffrey P. Gay, Estelle E. Ledoux, Matthias Krug, Julien Chantel, Anna Pakhomova, Carmen Sanchez-Valle, Sergio Speziale, Sébastien Merkel
Supervision: Sébastien Merkel
Writing – original draft: Jeffrey P. Gay

Abstract Seismic anisotropy is a powerful tool to map deformation processes in the deep Earth. Below 660 km, however, observations are scarce and conflicting. In addition, the underlying crystal scale mechanisms, leading to microstructures and crystal orientations, remain poorly constrained. Here, we use multigrain X-ray diffraction in the laser-heated diamond anvil cell to investigate the orientations of hundreds of grains in pyrolite, a model composition of the Earth's mantle, at in situ pressure and temperature. Bridgmanite in pyrolite exhibits three regimes of microstructures, due to transformation and deformation at low and high pressure. These microstructures result in predictions of 1.5%–2% shear wave splitting between 660 and 2,000 km with reversals in fast S-wave polarization direction at about 1,300 km depth. Anisotropy can develop in pyrolite at lower mantle conditions, but pressure has a significant impact on the plastic behavior of bridgmanite, and hence seismic observations, which may explain conflicting anisotropy observations.

Plain Language Summary Seismologists rely on observable data to construct models that describe the dynamic state of the Earth's lower mantle. These models, however, require constraints such as mantle composition and material behavior at high pressures and temperatures, which can be provided through experimental mineral physics. In this study, we use a high pressure devices and X-rays to impose deformation and image the state of our sample with increasing pressure and temperature. We are able to extract information of individual mineral grains within our assemblage, such as the number of grains per phase and their orientations. Using this experimental data, we identify three regimes of grain orientations in bridgmanite in the lower mantle, corresponding to transformation from lower pressure phases, and deformation at low and high pressure. With this information, we are able to make predictions about how seismic waves travel and behave based on the deformation state of the lower mantle.

1. Introduction

Pyrolite, a model mantle composition containing olivine, orthopyroxene, clinopyroxene, and garnet (Ringwood, 1962), is a model composition of the Earth's mantle (Irifune & Ringwood, 1987). Below 660 km depth, pyrolite consists predominately of (Mg,Fe)SiO_3 bridgmanite, $CaSiO_3$ davemaoite, and (Mg,Fe)O ferropericlase (Murakami et al., 2007; Komabayashi et al., 2010; X. Wang et al., 2015). Subjected to deformation, minerals in pyrolite could develop crystallographic preferred orientations (CPO) and be responsible for observations of seismic anisotropy (de Wit & Trampert, 2015; Ferreira et al., 2019; Wookey et al., 2002). If they do arise from CPO, our ability to interpret these seismic observations, however, relies on understanding texture development and active slip systems at appropriate conditions.

Experimentally, the development of texture requires deformation, preferably at mantle pressures and temperatures. The deformation behavior of bridgmanite (Cordier et al., 2004; Merkel et al., 2003; Miyagi & Wenk, 2016; Tsujino et al., 2016; Wenk et al., 2004), davemaoite (Immoor et al., 2022; Miyagi et al., 2009), and ferropericlase (Immoor et al., 2018; Merkel et al., 2002; Miyagi & Wenk, 2016) have been investigated under high pressures and, sometimes, high temperatures. These experiments have helped in constraining plasticity and deformation mechanisms in minerals (Cordier et al., 2004; Miyagi et al., 2010; Miyajima et al., 2009) with the addition of numerical models, allowing for studies on the effects of composition, temperature, and strain rate (Boioli et al., 2017; Carrez et al., 2007, 2017; Ferré et al., 2007; Mainprice et al., 2008) that cannot be addressed experimentally. Those, however, were not performed on a true pyrolitic composition, nor both at mantle pressures and temperatures and deserve a new investigation.

Writing – review & editing: Sébastien Merkel

Seismic observations indicate that the lower mantle appears largely isotropic (Chang et al., 2014; Meade et al., 1995) with observations of anisotropic structures heavily relying on corrections of crustal anisotropy (Panning et al., 2010). Additionally, observations of anisotropy in the lower mantle are rather weak (Montagner & Kennett, 1996; Ohuchi et al., 2011) with anisotropic anomalies largely confined to depths between 660 and 1,200 km (Ferreira et al., 2019), although there are reports of anisotropy below 1,900 km depth (de Wit & Trampert, 2015). It is debated whether dislocation creep is active in the lower mantle, with some suggesting it may be present (de Wit & Trampert, 2015; Ferreira et al., 2019) while others cite diffusion creep (Karato & Li, 1992) or dislocation climb (Boioli et al., 2017). If diffusion creep or dislocation climb are in fact dominant, one would expect little to no anisotropy as they are unlikely to produce CPO. However, there are regions with anisotropy that justify investigation of high pressure and temperature texture forming processes in pyrolitic materials in order to constrain mantle flow processes.

Here, we performed laser heated diamond anvil cell (LH-DAC) experiments on polycrystalline pyrolite. Multigrain X-ray crystallography (MGC) is employed to track the orientation of grains at pressures and temperatures relevant to conditions below the 660 km discontinuity down to 1,400 km. We report on experimental textures of bridgmanite, davemaoite, and ferropericlase. Previous work has demonstrated that strong transformation textures can be formed in bridgmanite upon synthesis (Gay et al., 2023b). This paper builds upon this expertise to demonstrate that deformation textures can be formed in bridgmanite at lower mantle pressures and temperatures, with an effect of depth and hydrostatic pressure. Visco-plastic self-consistent (VPSC) models are then used to determine the deformation mechanisms at play and identify an effect of pressure on the active slip systems in bridgmanite. Finally, we model P and S-wave anisotropy of pyrolite in the lower mantle.

2. Methods and Data Analysis

Three experimental runs were performed at the Extreme Conditions beamline P02.2 at PETRA III (DESY, Hamburg) using the same sample preparation and beamline setup outlined in Gay et al. (2023b) and shown in Figure 1a. Experiments for samples Pyr05 and Pyr07 used a monochromatic X-ray beam with a wavelength of 0.2898 Å, beam dimensions of 1.4 × 1.9 μm^2 (V × H FWHM), and a Perkin-Elmer XRD 1621 detector with 2,048 × 2,048 pixels and a 0.2 × 0.2 mm^2 pixel size. A CeO_2 powder standard from the National Institute of Standards and Technology (NIST; 674b) was used to calibrate detector tilt, beam center, and the sample to detector distance (551 mm). Sample Pyr01 was ran using an identical layout, a wavelength of 0.2904 Å, beam dimension of 1.2 × 1.9 μm^2 (V × H FWHM), and sample to detector distance of 403 mm. Double-sided laser heating was carried out using a Yb-fiber laser as installed by default on the beamline (Liermann et al., 2015). Raw data and calibration parameters can be found in Gay et al. (2023a).

Our starting material is a polycrystalline pyrolite sample, made from San-Carlos olivine, pyrope, enstatite, and diopside, sintered in a piston-cylinder apparatus at 2 GPa and 1,000°C for 30 min, cut into disks with a diamond wire saw, hand-polished to a thickness of ≈10 μm, coated on both sides with 500 nm of platinum, and cut into 20 μm diameter disks. More details and characterization of the starting material can be found in Gay et al. (2023b). Pyrolite disks are then loaded in 50–100 μm holes inside rhenium gaskets, with KCl as pressure medium for runs Pyr05 and Pyr07 and MgO for run Pyr01. Diamonds with a culet size of 250 μm diameter were used for runs Pyr05 and Pyr07, while run Pyr01 used beveled diamonds with 100 and 300 μm inner and outer diameters, respectively.

Our objective is to observe the evolution of texture during deformation at in situ pressures and temperatures of the Earth mantle. Pressure is increased at high temperature as close as possible to the mantle geotherm. Phases occurrence are identified using powder XRD and Dioptas (Prescher & Prakapenka, 2015). MGC data is then collected at ambient temperature by rotating the DAC in ω after quenching the sample to ambient temperature (Figure 1b).

The experiments start with the phase transformation; where ringwoodite and garnet decompose to form bridgmanite + davemaoite + ferropericlase. Errors in temperature for runs Pyr05 and Pyr07 are the deviation from the average values between the upstream and downstream temperatures. Errors in temperature for run Pyr01 are set to ±60 K due to insufficient temperature data collection during the experiment. Pressures in KCl (runs Pyr05 and Pyr07) and MgO (run Pyr01), are from HP-HT equations of state of Tateno et al. (2019) and Speziale et al. (2001), respectively.

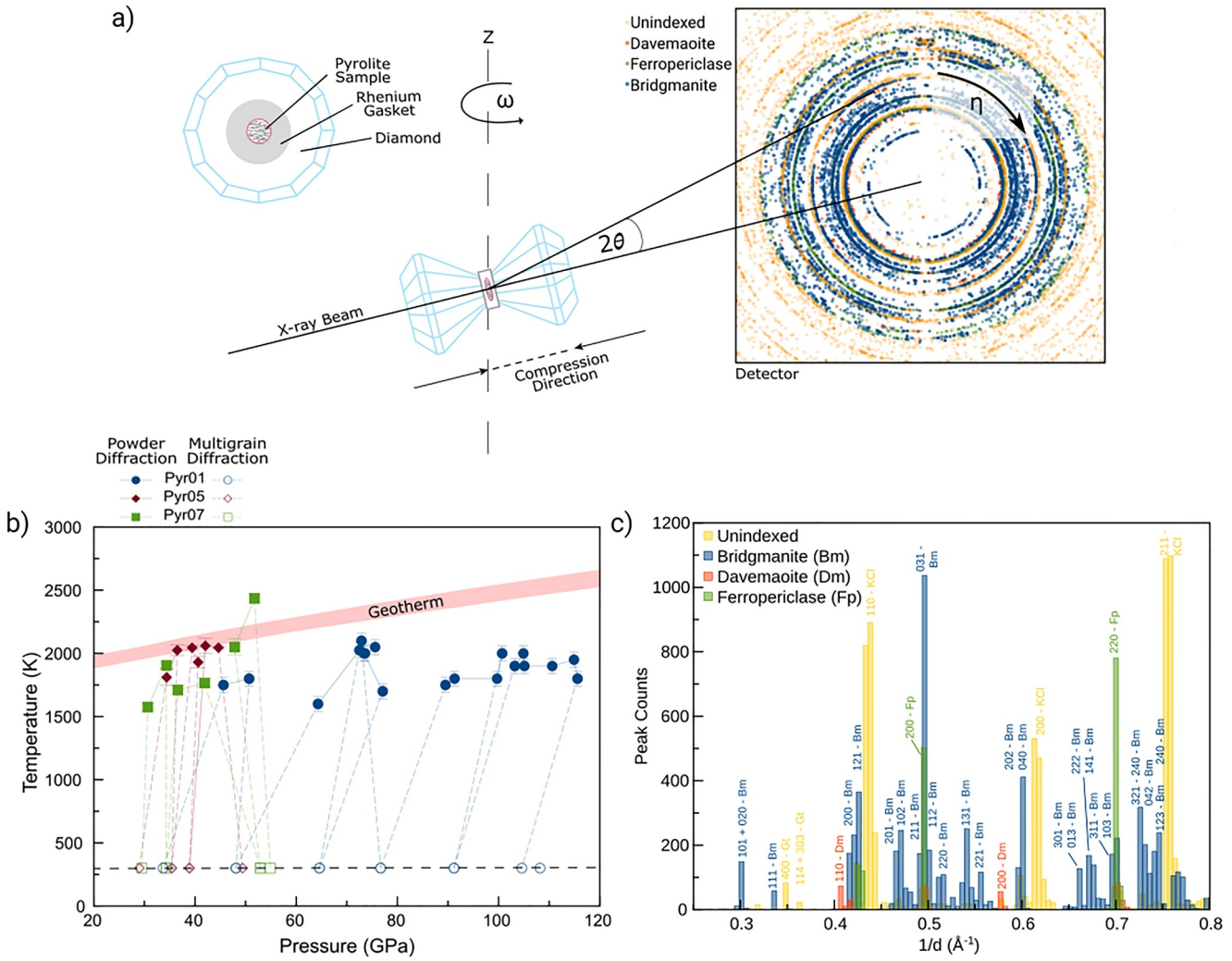

Figure 1. (a) Multigrain XRD setup. Pyrolite and KCl or MgO pressure mediums are loaded in a DAC. Multigrain X-ray diffraction is collected in steps of 0.5° as the assembly is rotated from −28° to 28° in ω. The inset shows peaks extracted from the diffraction images at 34 GPa in run Pyr05 with peaks assigned to bridgmanite in blue, davemaoite in orange, ferropericlase in green, and un-assigned in yellow. (b) P/T path for runs Pyr05, Pyr07, and Pyr01. Multigrain images are acquired at 300 K (open markers). Powder diffraction (filled markers) are collected at high temperature. Dotted lines denote when the sample is being heated or quenched. Red shaded area: geotherm from Katsura et al. (2010). (c) Histogram of the number of extracted single-grain diffraction peaks versus 1/d. The corresponding phase and Laue indices of each diffraction line are indicated. Un-indexed 2θ-ranges were ignored because of peak overlap with the pressure medium.

MGC images are collected by rotating the DAC in ω by 0.5° steps from −28° to 28° with collection times of 1 s per image. Figure 1c shows an example of a histogram of the number of extracted diffraction peaks against inverse d-spacing. Peaks from all phases can be clearly identified. Unit-cell parameters are then extracted using MAUD (Lutterotti et al., 1997) in Le Bail refinement mode where only unit-cell parameters are considered.

The indexing process uses open-source software from FABLE-3DXRD and the TIMEleSS-tools to clean raw diffraction images and extract a list of individual diffraction peaks. We then use ImageD11 to compute a list of **g**-vectors using the positions of diffraction peaks, refined unit cell parameters, and experimental conditions. In order to avoid incorrectly assigning pressure medium **g**-vectors to sample grains, 2θ ranges overlapping with the pressure medium are excluded from the list.

Finally, we use GrainSpotter (Schmidt, 2014) to index grains by assigning **g**-vectors with matching orientations. GrainSpotter generates a series of randomly oriented grains and computes their corresponding **g**-vectors. An experimental **g**-vector is assigned to a grain when the diffraction angles 2θ, η, and ω (Figure 1a) are within tolerances of the theoretical values. Indexed **g**-vectors are removed in subsequent indexings. The number of

indexed grains is improved by running between 50 and 100 iterations of GrainSpotter with increasing tolerances from $\sigma_{2\theta} = 0.02°$, $\sigma_{\eta} = 1.0°$, and $\sigma_{\omega} = 2.0°$ in the first iteration to $\sigma_{2\theta} = 0.08°$, $\sigma_{\eta} = 2.0°$, and $\sigma_{\omega} = 3.0°$ in the last iteration.

Strain rate and stress are difficult to determine in DAC experiments. We do not know the total applied strain. Nevertheless, we can compare our experimental texture strength with VPSC simulations (see below): axial strain is set to 30%–70% in the simulations and provides a good match to the experimental textures. Considering each experiment takes 3–12 hr to complete, strain rates are hence on the order of 1×10^{-5} to 5×10^{-5} s^{-1}. Stress determination, although theoretically possible, proves difficult. For one, diffraction patterns of the phases of interest are individual diffraction spots, incompatible with classic powder diffraction analysis for stress determination. Additionally, because we use an axial geometry, determination of stress relies on tracking small shifts in peak positions. We attempted to rely on the pressure medium (KCl or MgO), which results in more powder-like diffraction. The fit quality, however, was inconsistent and not reproducible. Stress values are, hence, not reported here.

3. Results

3.1. Grain Indexing Statistics

Grains orientations for all phases are indexed simultaneously: bridgmanite, davemaoite, and ferropericlase in runs Pyr05 and Pyr07 and only bridgmanite and davemaoite for Pyr01, as MgO was used as a pressure medium. We are able to index between 107 and 442 grains in bridgmanite, 4 to 182 grains of davemaoite, and 2 to 272 grains of ferropericlase in a multiphase material. Indexing capabilities decrease with increasing pressure due to higher strains applied to the sample. Full results on grain indexing capabilities are not the main point of this paper and will not be discussed further. They are provided in Tables S1–S3 in Supporting Information S1.

3.2. Deformation Textures in Bridgmanite

We do not observe textures or consistent texture development in davemaoite and ferropericlase. Hence, only bridgmanite, which makes up over 75% of our sample, will be discussed. All measured texture plots for all phase are shown in Figures S1–S3 in Supporting Information S1. Representative results for bridgmanite are shown in Figure 2. Pyr07 represents deformation at lower pressures, below 55 GPa, while Pyr01 is representative of higher pressures, exceeding 100 GPa.

Bridgmanite displays a strong 001 texture upon transformation. In run Pyr07, we then observe the reorientation to (100) planes perpendicular to compression and the maximum at 001 begins to weaken. Eventually, at 55 GPa, orientations form a girdle between 100 and 010, with a persisting weak maximum at 001. Run Pyr01 begins at 34 GPa with a strong maximum in 001, which weakens, and gains a secondary maximum at 010. At 65 GPa the maximum at 001 is gone, leaving a strong orientation of (010) planes perpendicular to compression. Texture then remains largely unchanged until above 100 GPa.

3.3. Plasticity of Bridgmanite at Lower Mantle P/T Conditions

We interpret our results in terms of dominant deformation mechanisms using VPSC modeling, adjusting models and slip system combinations from the literature on bridgmanite (Couper et al., 2020; Hirel et al., 2014; Kasemer et al., 2020; Mainprice et al., 2008; Miyagi & Wenk, 2016; Tsujino et al., 2016). Our preferred models are shown in Table 1, along with the corresponding critical resolved shear stresses (CRSS) and slip activity. VPSC modeling was carried out in two stages to produce the two observed textures (Figure 2), representing deformation in low pressure and high pressure regimes. Starting from a 001 transformation texture, we allow slip along (100)[010] and (100)[001] at 30% strain to deplete 001 orientations while generating a weak 100 texture. In the second stage, we allow slip along (010)⟨101⟩, (010)[100], and (010)[001] to produce a concentrated 010 texture when strained to 70%. Texture in davemaoite does not evolve with deformation and ferropericlase remains isotropic. Adding these phases in VPSC will not impact our results.

3.4. Seismic Anisotropy

Wave velocities are calculated with MTEX (Bachmann et al., 2010; Mainprice et al., 2014). For bridgmanite we interpolate single-crystal elastic constants from first principles calculations (Luo et al., 2021) at 27 GPa/1900 K

10.1029/2024GL109433

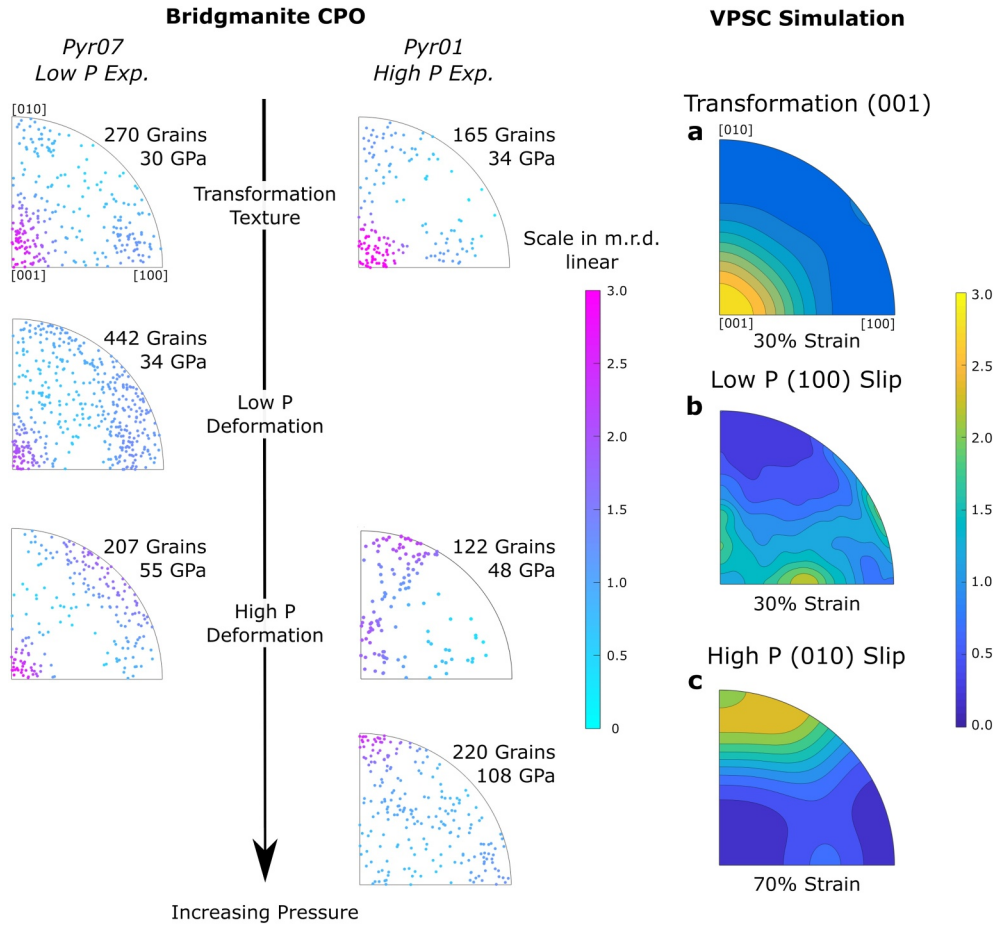

Figure 2. (left) Inverse pole figures (IPF) of the compression direction, showing individual bridgmanite grain orientations in pyrolite versus pressures. Equal area projection. Grains are colored according to an orientation distribution fitted to the grain orientations and color scale in multiples of random distribution (m.r.d.). (right) IPF (a–c) for axial compression VPSC simulation. Starting from transformation texture (a) applying 30% axial strain and allowing dominant slip on (100) planes (b). Second stage of deformation (c) starting from (b), allowing 70% total strain with dominant slip along (010) planes.

and 88 GPa/2260 K, corresponding to 750 and 2,030 km depth, respectively. Transformation is prescribed to replicate the experimental transformation texture. Below the 660 km discontinuity, deformation is modeled in simple shear up to 100% starting from a random texture and the two plastic models of Table 1 (Figure S4 in Supporting Information S1). A simple shear geometry is efficient to understand the relation between deformation and seismic anisotropy while avoiding complex convection models. The contributions of ferropericlase and davemaoite are assumed isotropic based on the lack of texture in our experiment. Nevertheless, they contribute to average seismic velocities in the pyrolite polycrystal. We hence account for their contributions using isotropic elastic constants, densities, and phase proportions calculated using the HeFESTo thermodynamic model (Stixrude & Lithgow-Bertelloni, 2010). MTEX is then used to compute the velocities in a pyrolite polycrystal.

The resulting polycrystal anisotropy of pyrolite is shown in Figure 3 with all corresponding densities, single crystal, and polycrystal elastic moduli in Table S4. We identify three regimes:

- Upon transformation at the 660 discontinuity, we predict up to 1.5% S-wave splitting for waves traveling perpendicular to compression with a fast polarization parallel to compression. Mean P-wave velocity is 10.9 km/s with a maximum at approximately 45° to compression and 0.3% P-wave anisotropy.
- Shear at depth of around 750 km also results in approximately 1.5% maximum shear wave splitting, but with the fast polarization direction sub-parallel for waves traveling in the shear plane. Mean V_P is 10.9 km/s and the velocity is maximum for waves traveling sub-parallel to the shear plane, with 1.4% P-wave anisotropy.

Table 1
Relative CRSS and Slip System Activity in Bridgmanite Modeled Using VPSC

	Low P		High P	
Slip system	CRSS	Activity (%)	CRSS	Activity (%)
(100)[010]	2	18.0	4	0.6
(100)[001]	1	34.7	4	9.0
(100)⟨011⟩	3	6.0	5	5.9
(010)[100]	4	2.2	1	36.9
(010)[001]	2	11.3	1	34.4
(010)⟨101⟩	3	9.4	4	1.4
(001)[100]	2	4.3	5	4.6
(001)[010]	2	11.3	3	1.3
(001)⟨110⟩	5	1.2	5	4.3
{111}⟨110⟩	30	1.6	30	1.6

Note. Two stages of compression are performed in order to recreate the textures observed in the experimental data. VPSC texture comparisons only constrain relative CRSS values.

- Finally, for shear at depth of around 2,030 km, we predict up to 2.0% shear wave splitting with the fast polarization direction nearly orthogonal to the shear plane for waves traveling in the shear plane. Mean V_P is 12.9 km/s with 2.9% P-wave anisotropy.

4. Discussion

4.1. Plastic Behavior of Bridgmanite Within a Pyrolitic Composition

While many studies have investigated deformation textures and mechanisms in bridgmanite (e.g., Boioli et al., 2017; Cordier et al., 2004; Ferré et al., 2007; Kraych et al., 2016; Mainprice et al., 2008; Merkel et al., 2003; Miyagi & Wenk, 2016; Y. Wang et al., 1992; Wenk et al., 2004, 2006), and others taking into consideration aggregates (Couper et al., 2020; Girard et al., 2016; Kaercher et al., 2016), none have studied the deformation of bridgmanite within a pyrolitic composition. According to shear deformation experiments by Tsujino et al. (2016), the most active slip system is (100)[001] at 25 GPa and 1872 K, which is in relative agreement with Peierls-Nabarro numerical modeling by Mainprice et al. (2008), who finds (100)[010] to be the most active. Also in agreement are DAC deformation experiments by Couper et al. (2020) who find that at shallow lower mantle conditions, slip activity is split between (100)[010] and (100)[001] or (100)⟨011⟩. Our VPSC simulations for the first deformation stage, below 50 GPa, predict dominant slip

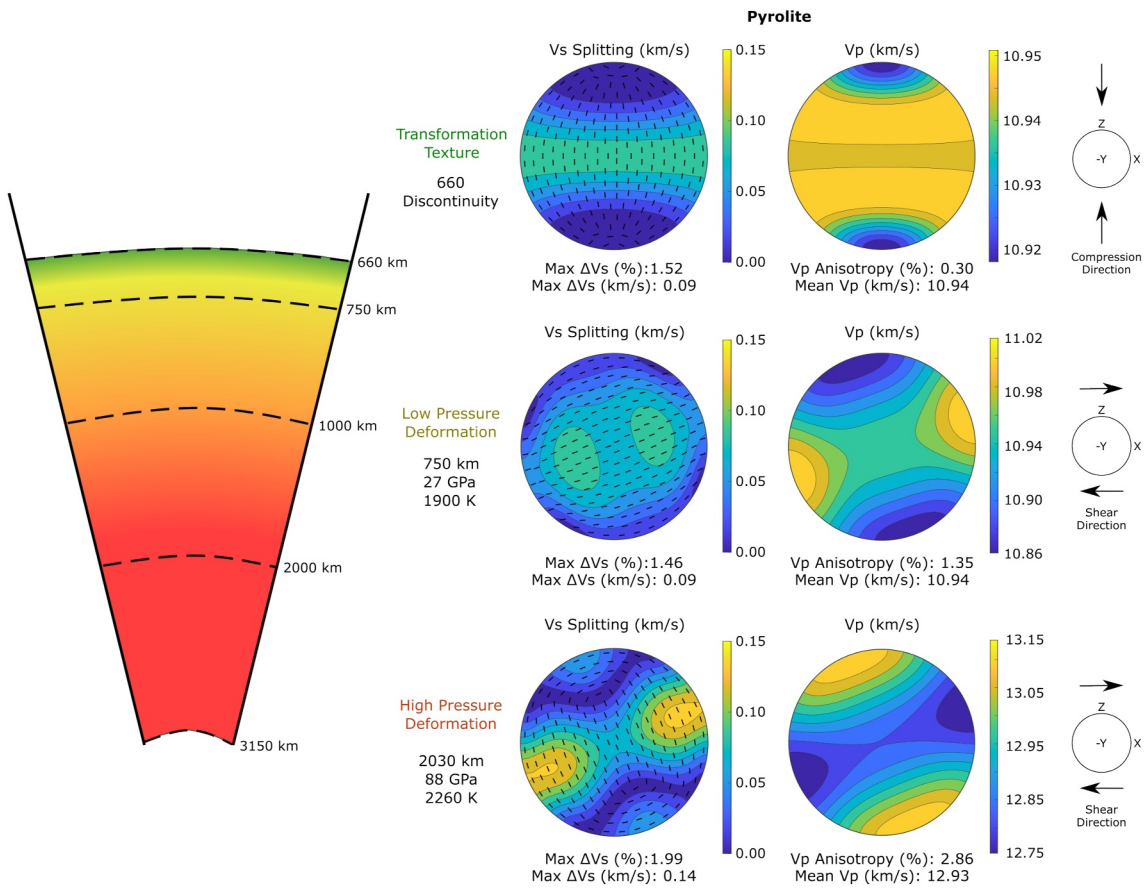

Figure 3. Seismic velocities in polycrystalline pyrolite upon transformation at 660 km, and deformation at both 745 and 2,030 km depth. Black tick marks in V_S splitting plots indicate the fast wave polarization direction. Wedge cut out of the Earth's mantle highlights the depth range of the three proposed scenarios: phase transformation, low pressure deformation, and high pressure deformation. Corresponding figures for pure bridgmanite are available in Supporting Information S1.

activity (34.7%) on (100)[001] with minor contributions (18.0%) from (100)[010] and (11.3%) from (010)[001] and (001)[010] and are hence in agreement with findings of Tsujino et al. (2016) and Couper et al. (2020). This confirms that (100)[001] controls the development of orientations in bridgmanite from deformation at somewhat shallow depth.

(010) dislocations and the presence of twinning were inferred from a sample of bridgmanite deformed at 27 GPa and 2130 K (Nzogang et al., 2018). Slip along (010) is in fact active in this pressure range, but does not seem to control the development of texture. Our experimental results do not show evidence of twinning. Twinning induces a fast reorientation of grains for $NaCoF_3$ perovskite (Gay et al., 2021), which is not observed here.

In addition to (100)[001] slip at shallow lower mantle conditions, we also observe an effect of pressure with a gradual shift toward a regime in which slip on (010) becomes dominant. This effect of hydrostatic pressure had been predicted using Peierls stress and CRSS calculations (Hirel et al., 2014; Kraych et al., 2016), with a transition between easier slip on (100)[010] at 30 GPa and on (010)[100] once pressures exceed 60 GPa. These results compare well to our results, where we observe an increased activity of (010) slip at pressures above approximately 50 GPa.

We have hence experimentally identified two main deformation regimes. The first occurs below approximately 50 GPa, corresponding to approximately 1,300 km depth, where (100)[001] is the dominant slip system. At pressures exceeding approximately 50 GPa, a shift in dominant slip system occurs where (010)[100] and (010)[001] become most active. We hence suggest that pressure has a significant impact on the plastic behavior of bridgmanite within a pyrolitic material, resulting in a smooth transition of dominant slip system around 1,300 km depth.

4.2. Implications for Earth's Lower Mantle

We identify three scenarios for pyrolite anisotropy from bridgmanite in the Earth's lower mantle (Figure 3). We begin with a strong 001 transformation texture at 660 km depth that could be the result of a subducting oceanic slab generating a compressive force on the more viscous underlying mantle (Gay et al., 2023b). Below, we predict a change in dominant slip systems of bridgmanite at around 1,300 km depth. We then study the cases of horizontal shear deformation above and below 1,300 km depth.

Maximum shear wave splitting is 1.5%–2% in or near the horizontal plane for all scenarios. Polarization direction, however, changes with depth. After transformation, vertically polarized shear waves (V_{SV}) lead horizontally polarized shear waves (V_{SH}) for waves traveling parallel to the shear plane ($V_{SV} > V_{SH}$). At 750 km depth, deformation induces a change in the fast polarization direction with $V_{SH} > V_{SV}$. Finally, we again find $V_{SV} > V_{SH}$ for waves traveling in the shear plane at 2,030 km depth.

Seismological studies report strong anisotropy in some regions of the lower mantle (Ferreira et al., 2019; Wookey et al., 2002), while the overall mantle appears largely isotropic (Meade et al., 1995; Panning & Romanowicz, 2006). Our predictions of 2% maximum shear wave splitting is consistent with studies reporting local observations of anisotropy. Additionally, within our model, studies with nearly vertical SKS waves will cross regions with both $V_{SV} > V_{SH}$ and $V_{SH} > V_{SV}$ that will hence cancel each other. Reports of no global anisotropy using SKS waves is hence also consistent with our results. Finally, the predicted 1.5%–2% V_S anisotropy is much weaker compared to what is reported at shallower depths (Dziewonski & Anderson, 1981; Mainprice, 2007; Montagner & Kennett, 1996; Silver, 1996) or near D" (Long & Becker, 2010; Panning & Romanowicz, 2004; Wookey & Kendall, 2007) and may be difficult to extract in seismological studies.

Evidence for lower mantle anisotropy generally comes from shear and surface waves (Wookey & Kendall, 2007). Nevertheless, we report on P-wave anisotropy with a marked increase in anisotropy from 1.4% to 2.9% with increasing depth. Additionally, we predict a reversal in fast propagation direction of P-waves from sub-parallel to sub-orthogonal to shear (a change of 90°) with depth. This predicted increase in anisotropy with depth is consistent with the observations of de Wit and Trampert (2015).

5. Conclusions

This work implements in situ multigrain X-ray diffraction experiments to observe the development of microstructures in a pyrolitic material at lower mantle pressures and temperatures. We use the observed textures to

identify the active deformation mechanisms in bridgmanite, the dominant phase in pyrolite at lower mantle conditions. We identify three regimes of texture: transformation texture due to stress, deformation at low pressure and deformation at high pressure, with a smooth transition between the two plastic regimes in the vicinity of 50 GPa or 1,300 km depth in the Earth mantle.

Based on our results, we model anisotropy in pyrolite at lower mantle conditions. There are three regimes, just below the 660 km discontinuity, due to transformation microstructures, and at depths above and below approximately 1,300 km due to deformation. At all depths, shear wave splitting reaches up to 1.5%–2%, with a depth dependence of orientations of the fast shear wave polarization. P-wave anisotropy increases from 1.4% below the 660 km discontinuity to 2.9% at 1,300 km with fast travel direction flipping from sub-parallel to sub-orthogonal to the shear plane.

This work provides long-expected inputs that were otherwise absent in current models of plastic deformation and anisotropy in the Earth's lower mantle. With this information, we can now couple our results with more realistic geodynamic models. We will then be able to compare these updated models to real world observations, providing a better view of flow in the deep Earth, in order to better understand the dynamic evolution of the Earth's mantle.

Data Availability Statement

Data files necessary for grain indexing are available on Recherche Data Gouv (Gay et al., 2023a). For each pressure and each run, we provide the raw diffraction images, the list of peaks extracted from the diffraction images, a calibration file, and crystallographic information for the phases we indexed. The archive also provides the list of indexed grains and their orientations for all phases and all pressures as well as the input files to reproduce the VPSC simulations. Raw data for single and polycrystal elastic properties are provided in Table S4. Software for processing the multigrain X-ray diffraction data are all open source, part of the Fable-3DRXD and TIMEleSS packages (Fable-3DRXD community, 2024). A guide for multigrain XRD data processing was written in the course of the ANR-DFG TIMEleSS project and is available at http://multigrain.texture.rocks/. Other software we use are the open-source MTEX (MTEX community, 2024) and MAUD (Lutterotti, 2024).

Acknowledgments
The study was financed by the bilateral ANR-DFG TIMEleSS project (ANR-17-CE31-0025; TH 1530/18-1; SA 2585/3-1; SP1216/8-1) and the bilateral PROCOPE-PPP program (Campus France PHC 40555PC; DAAD 57390184). The Chevreul Institute and the Lille Electron Microscopy Platform are thanked for their help in the development of this work through the ARCHI-CM project supported by the "Ministère de l'Enseignement Supérieur de la Recherche et de l'Innovation," the région "Hauts-de-France," the ERDF program of the European Union and the "Métropole Européenne de Lille." This research was carried out at the P02.2 beamline of the PETRA III synchrotron at DESY, a member of the Helmholtz Association (HGF). The research leading to this result has been supported by the project CALIPSOplus under the Grant 730872 from the EU Framework Programme for Research and Innovation HORIZON 2020. We also thank the staff from the Extreme Conditions Lab at IMPMC Sorbonne Université in Paris for assistance with the laser machining of samples and Hanns-Peter Liermann at DESY for assistance during the experiment.

References

Bachmann, F., Hielscher, R., & Schaeben, H. (2010). Texture analysis with MTEX- Free and open source software toolbox. *Solid State Phenomena*, *160*, 63–68. https://doi.org/10.4028/www.scientific.net/SSP.160.63

Boioli, F., Carrez, P., Cordier, P., Devincre, B., Gouriet, K., Hirel, P., et al. (2017). Pure climb creep mechanism drives flow in Earth's lower mantle. *Science Advances*, *3*(3), 1–7. https://doi.org/10.1126/sciadv.1601958

Carrez, P., Ferré, D., & Cordier, P. (2007). Implications for plastic flow in the deep mantle from modelling dislocations in $MgSiO_3$ minerals. *Nature*, *446*(7131), 68–70. https://doi.org/10.1038/nature05593

Carrez, P., Goryaeva, A. M., & Cordier, P. (2017). Prediction of mechanical twinning in magnesium silicate post- perovskite. *Scientific Reports*, *7*, 1–9. https://doi.org/10.1038/s41598-017-18018-1

Chang, S. J., Ferreira, A. M., Ritsema, J., Van Heijst, H. J., & Woodhouse, J. H. (2014). Global radially anisotropic mantle structure from multiple datasets: A review, current challenges, and outlook. *Tectonophysics*, *617*, 1–19. https://doi.org/10.1016/j.tecto.2014.01.033

Cordier, P., Ungár, T., Zsoldos, L., & Tichy, G. (2004). Dislocation creep in $MgSiO_3$ perovskite at conditions of the Earth's uppermost lower mantle. *Nature*, *428*(1), 837–840. https://doi.org/10.1038/nature02472

Couper, S., Speziale, S., Marquardt, H., Liermann, H. P., & Miyagi, L. (2020). Does heterogeneous strain act as a control on seismic anisotropy in Earth's lower mantle? *Frontiers in Earth Science*, *8*, 1–20. https://doi.org/10.3389/feart.2020.540449

de Wit, R., & Trampert, J. (2015). Robust constraints on average radial lower mantle anisotropy and consequences for composition and texture. *Earth and Planetary Science Letters*, *429*, 101–109. https://doi.org/10.1016/j.epsl.2015.07.057

Dziewonski, A. M., & Anderson, D. L. (1981). Preliminary reference Earth model. *Physics of the Earth and Planetary Interiors*, *25*(4), 297–356. https://doi.org/10.1016/0031-9201(81)90046-7

Fable-3DRXD community. (2024). Fable-3DRXD [Software]. *GitHub*. Retrieved from https://github.com/FABLE-3DXRD

Ferré, D., Carrez, P., & Cordier, P. (2007). First principles determination of dislocations properties of $MgSiO_3$ perovskite at 30 GPa based on the Peierls-Nabarro model. *Physics of the Earth and Planetary Interiors*, *163*(1–4), 283–291. https://doi.org/10.1016/j.pepi.2007.05.011

Ferreira, A. M., Faccenda, M., Sturgeon, W., Chang, S. J., & Schardong, L. (2019). Ubiquitous lower-mantle anisotropy beneath subduction zones. *Nature Geoscience*, *12*(4), 301–306. https://doi.org/10.1038/s41561-019-0325-7

Gay, J. P., Ledoux, E., Krug, M., Chantel, J., Pakhomova, A., Liermann, H.-P., et al. (2023a). Dataset for "depth dependent deformation and anisotropy of pyrolite in the Earth's lower mantle" [Dataset]. *Recherche Data Gouv*. https://doi.org/10.57745/VM1WZW

Gay, J. P., Ledoux, E., Krug, M., Chantel, J., Pakhomova, A., Liermann, H.-P., et al. (2023b). Transformation microstructures in pyrolite under stress: Implications for anisotropy in subducting slabs below the 660 km discontinuity. *Earth and Planetary Science Letters*, *604*, 118015. https://doi.org/10.1016/j.epsl.2023.118015

Gay, J. P., Miyagi, L., Couper, S., Langrand, C., Dobson, D. P., Liermann, H.-P., & Merkel, S. (2021). Deformation of NaCoF3 perovskite and post-perovskite up to 30 GPa and 1013 K: Implications for plastic deformation and transformation mechanism. *European Journal of Mineralogy*, *33*(5), 591–603. https://doi.org/10.5194/ejm-33-591-2021

Girard, J., Amulele, G., Farla, R., Mohiuddin, A., & Karato, S. I. (2016). Shear deformation of bridgmanite and magnesiowüstite aggregates at lower mantle conditions. *Science*, *351*(6269), 144–147. https://doi.org/10.1126/science.aad3113

Hirel, P., Kraych, A., Carrez, P., & Cordier, P. (2014). Atomic core structure and mobility of [100](010) and [010](100) dislocations in $MgSiO_3$ perovskite. *Acta Materialia*, *79*, 117–125. https://doi.org/10.1016/j.actamat.2014.07.001

Immoor, J., Marquardt, H., Miyagi, L., Lin, F., Speziale, S., Merkel, S., et al. (2018). Evidence for {100}⟨011⟩ slip in ferropericlase in Earth's lower mantle from high-pressure/high-temperature experiments. *Earth and Planetary Science Letters*, *489*, 251–257. https://doi.org/10.1016/j.epsl.2018.02.045

Immoor, J., Miyagi, L., Liermann, H.-P., Speziale, S., Schulze, K., Buchen, J., et al. (2022). Weak cubic $CaSiO_3$ perovskite in the Earth's mantle. *Nature*, *603*(7900), 276–279. https://doi.org/10.1038/s41586-021-04378-2

Irifune, T., & Ringwood, A. E. (1987). In *Phase transformations in primitive MORB and pyrolite compositions to 25 gpa and some geophysical implications* (Vol. 39).

Kaercher, P., Miyagi, L., Kanitpanyacharoen, W., Zepeda-Alarcon, E., Wang, Y., Parkinson, D., et al. (2016). Two-phase deformation of lower mantle mineral analogs. *Earth and Planetary Science Letters*, *456*, 134–145. https://doi.org/10.1016/j.epsl.2016.09.030

Karato, S.-I., & Li, P. (1992). Diffusion creep in perovskite: Implications for the rheology of the lower mantle. *Science*, *255*(5049), 1238–1240. https://doi.org/10.1126/science.255.5049.1238

Kasemer, M., Zepeda-Alarcon, E., Carson, R., Dawson, P., & Wenk, H. R. (2020). Deformation heterogeneity and intragrain lattice misorientation in high strength contrast, dual-phase bridgmanite/periclase. *Acta Materialia*, *189*, 284–298. https://doi.org/10.1016/j.actamat.2020.02.061

Katsura, T., Yoneda, A., Yamazaki, D., Yoshino, T., Ito, E., Suetsugu, D., & Jellinek, M. (2010). Adiabatic temperature profile in the mantle. *Physics of the Earth and Planetary Interiors*, *183*(1–2), 212–218. https://doi.org/10.1016/j.pepi.2010.07.001

Komabayashi, T., Hirose, K., Nagaya, Y., Sugimura, E., & Ohishi, Y. (2010). High-temperature compression of ferropericlase and the effect of temperature on iron spin transition. *Earth and Planetary Science Letters*, *297*(3–4), 691–699. https://doi.org/10.1016/j.epsl.2010.07.025

Kraych, A., Carrez, P., & Cordier, P. (2016). On dislocation glide in $MgSiO_3$ bridgmanite at high-pressure and high-temperature. *Earth and Planetary Science Letters*, *452*, 60–68. https://doi.org/10.1016/j.epsl2016.07.035

Liermann, H. P., Konôpková, Z., Morgenroth, W., Glazyrin, K., Bednarčik, J., McBride, E. E., et al. (2015). The extreme conditions beamline P02.2 and the extreme conditions science infrastructure at PETRA III. *Journal of Synchrotron Radiation*, *22*(4), 908–924. https://doi.org/10.1107/S1600577515005937

Long, M. D., & Becker, T. W. (2010). Mantle dynamics and seismic anisotropy. *Earth and Planetary Science Letters*, *297*(3–4), 341–354. https://doi.org/10.1016/j.epsl.2010.06.036

Luo, C., Deng, X., Wang, W., Shukla, G., Wu, Z., & Wentzcovitch, R. M. (2021). cij: A Python code for quasiharmonic thermoelasticity. *Computer Physics Communications*, *267*, 108067. https://doi.org/10.1016/j.cpc.2021.108067

Lutterotti, L. (2024). MAUD—Materials analysis using diffraction [Software]. *GitHub*. Retrieved from https://luttero.github.io/maud/

Lutterotti, L., Matthies, S., Wenk, H. R., Schultz, A. S., & Richardson, J. W. (1997). Combined texture and structure analysis of deformed limestone from time-of-flight neutron diffraction spectra. *Journal of Applied Physics*, *81*(2), 594–600. https://doi.org/10.1063/1.364220

Mainprice, D. (2007). Seismic anisotropy of the deep Earth from a mineral and rock physics perspective. *Treatise on Geophysics*, *2*, 437–491. https://doi.org/10.1016/B978-044452748-6.00045-6

Mainprice, D., Bachmann, F., Hielscher, R., & Schaeben, H. (2014). Descriptive tools for the analysis of texture projects with large datasets using MTEX: Strength, symmetry and components. *Geological Society - Special Publications*, *409*(1), 251–271. https://doi.org/10.1144/SP409.8

Mainprice, D., Tommasi, A., Ferré, D., Carrez, P., & Cordier, P. (2008). Predicted glide systems and crystal preferred orientations of polycrystalline silicate Mg-Perovskite at high pressure: Implications for the seismic anisotropy in the lower mantle. *Earth and Planetary Science Letters*, *271*(1–4), 135–144. https://doi.org/10.1016/j.epsl.2008.03.058

Meade, C., Silver, P. G., & Kaneshima, S. (1995). Laboratory and seismological observations of lower mantle isotropy. *Geophysical Research Letters*, *22*(10), 1293–1296. https://doi.org/10.1029/95GL01091

Merkel, S., Wenk, H. R., Badro, J., Montagnac, G., Gillet, P., Mao, H. K., & Hemley, R. J. (2003). Deformation of $(Mg_{0.9},Fe_{0.1})SiO_3$ perovskite aggregates up to 32 GPa. *Earth and Planetary Science Letters*, *209*(3–4), 351–360. https://doi.org/10.1016/S0012-821X(03)00098-0

Merkel, S., Wenk, H. R., Shu, J., Shen, G., Gillet, P., Mao, H.-K., & Hemley, R. J. (2002). Deformation of polycrystalline MgO at pressures of the lower mantle. *Journal of Geophysical Research*, *107*(B11), ECV3-1–ECV3-17. https://doi.org/10.1029/2001jb000920

Miyagi, L., Kanitpanyacharoen, W., Kaercher, P., Lee, K. K., & Wenk, H. R. (2010). Slip systems in $MgSiO_3$ post-perovskite: Implications for D anisotropy. *Science*, *329*(5999), 1639–1641. https://doi.org/10.1126/science.1192465

Miyagi, L., Merkel, S., Yagi, T., Sata, N., Ohishi, Y., & Wenk, H. R. (2009). Diamond anvil cell deformation of $CaSiO_3$ perovskite up to 49 GPa. *Physics of the Earth and Planetary Interiors*, *174*(1–4), 159–164. https://doi.org/10.1016/j.pepi.2008.05.018

Miyagi, L., & Wenk, H. R. (2016). Texture development and slip systems in bridgmanite and bridgmanite + ferropericlase aggregates. *Physics and Chemistry of Minerals*, *43*(8), 597–613. https://doi.org/10.1007/s00269-016-0820-y

Miyajima, N., Yagi, T., & Ichihara, M. (2009). Dislocation microstructures of $MgSiO_3$ perovskite at a high pressure and temperature condition. *Physics of the Earth and Planetary Interiors*, *174*(1–4), 153–158. https://doi.org/10.1016/j.pepi.2008.04.004

Montagner, J. P., & Kennett, B. L. (1996). How to reconcile body-wave and normal-mode reference earth models. *Geophysical Journal International*, *125*(1), 229–248. https://doi.org/10.1111/j.1365-246X.1996.tb06548.x

MTEX community. (2024). MTEX, a free Matlab toolbox for analyzing and modeling crystallographic textures [Software]. *GitHub*. Retrieved from https://mtex-toolbox.github.io/

Murakami, M., Sinogeikin, S. V., Bass, J. D., Sata, N., Ohishi, Y., & Hirose, K. (2007). Sound velocity of $MgSiO_3$ post-perovskite phase: A constraint on the D discontinuity. *Earth and Planetary Science Letters*, *259*(1–2), 18–23. https://doi.org/10.1016/j.epsl.2007.04.015

Nzogang, B. C., Bouquerel, J., Cordier, P., Mussi, A., Girard, J., & Karato, S. (2018). Characterization by scanning precession electron diffraction of an aggregate of bridgmanite and ferropericlase deformed at hp-ht. *Geochemistry, Geophysics, Geosystems*, *19*(3), 582–594. https://doi.org/10.1002/2017GC007244

Ohuchi, T., Kawazoe, T., Nishihara, Y., Nishiyama, N., & Irifune, T. (2011). High pressure and temperature fabric transitions in olivine and variations in upper mantle seismic anisotropy. *Earth and Planetary Science Letters*, *304*(1–2), 55–63. https://doi.org/10.1016/j.epsl.2011.01.015

Panning, M., Lekić, V., & Romanowicz, B. A. (2010). Importance of crustal corrections in the development of a new global model of radial anisotropy. *Journal of Geophysical Research*, *115*(12), 1–18. https://doi.org/10.1029/2010JB007520

Panning, M., & Romanowicz, B. (2004). Inferences on flow at the base of Earth's mantle based on seismic anisotropy. *Science*, *303*(5656), 351–353. https://doi.org/10.1126/science.1091524

Panning, M., & Romanowicz, B. (2006). A three-dimensional radially anisotropic model of shear velocity in the whole mantle. *Geophysical Journal International*, *167*(1), 361–379. https://doi.org/10.1111/j.1365-246X.2006.03100.x

Prescher, C., & Prakapenka, V. B. (2015). DIOPTAS: A program for reduction of two-dimensional X-ray diffraction data and data exploration. *High Pressure Research*, *35*(3), 223–230. https://doi.org/10.1080/08957959.2015.1059835

Ringwood, A. E. (1962). A model for the layered upper mantle. *Journal of Geophysical Research*, *67*(2), 857–867. https://doi.org/10.1029/JZ067i002p00857

Schmidt, S. (2014). GrainSpotter: A fast and robust polycrystalline indexing algorithm. *Journal of Applied Crystallography*, *47*(1), 276–284. https://doi.org/10.1107/S1600576713030185

Silver, P. G. (1996). Seismic anisotropy beneath the continents: Probing the depths of geology. *Annual Review of Earth and Planetary Sciences*, *24*(1), 385–432. https://doi.org/10.1146/annurev.earth.24.1.385

Speziale, S., Zha, C. S., Duffy, T. S., Hemley, R. J., & Mao, H.-K. (2001). Quasi-hydrostatic compression of magnesium oxide to 52 GPa: Implications for the pressure-volume-temperature equation of state. *Journal of Geophysical Research*, *106*(2000), 515–528. https://doi.org/10.1029/2000jb900318

Stixrude, L., & Lithgow-Bertelloni, C. (2010). Thermodynamics of mantle minerals—II. Phase equilibria. *Geophysical Journal International*, *184*(3), 1180–1213. https://doi.org/10.1111/j.1365-246X.2010.04890.x

Tateno, S., Komabayashi, T., Hirose, K., Hirao, N., & Ohishi, Y. (2019). Static compression of B2 KCl to 230 GPa and its. *American Mineralogist*, *104*(May), 718–723. https://doi.org/10.2138/am-2019-6779

Tsujino, N., Nishihara, Y., Yamazaki, D., Seto, Y., Higo, Y., & Takahashi, E. (2016). Mantle dynamics inferred from the crystallographic preferred orientation of bridgmanite. *Nature*, *539*(7627), 81–84. https://doi.org/10.1038/nature19777

Wang, X., Tsuchiya, T., & Hase, A. (2015). Computational support for a pyrolitic lower mantle containing ferric iron. *Nature Geoscience*, *8*(7), 556–559. https://doi.org/10.1038/ngeo2458

Wang, Y., Guyot, F., & Liebermann, R. C. (1992). Electron microscopy of (Mg,Fe)SiO_3 perovskite: Evidence for structural phase transitions and implications for the lower mantle. *Journal of Geophysical Research*, *97*(B9), 327–347. https://doi.org/10.1029/92jb00870

Wenk, H. R., Lonardeli, I., Pehl, J., Devine, J., Prakapenka, V., Shen, G., & Mao, H. K. (2004). In situ observation of texture development in olivine, ringwoodite, magnesiowüstite and silicate perovskite at high pressure. *Earth and Planetary Science Letters*, *226*(3–4), 507–519. https://doi.org/10.1016/j.epsl.2004.07.033

Wenk, H. R., Lonardelli, I., Merkel, S., Miyagi, L., Pehl, J., Speziale, S., & Tommaseo, C. E. (2006). Deformation textures produced in diamond anvil experiments, analysed in radial diffraction geometry. *Journal of Physics: Condensed Matter*, *18*(25), S933–S947. https://doi.org/10.1088/0953-8984/18/25/S02

Wookey, J., & Kendall, J. M. (2007). Seismic anisotropy of post-perovskite and the lowermost mantle. https://doi.org/10.1029/174GM13

Wookey, J., Kendall, J. M., & Barruol, G. (2002). Mid-mantle deformation inferred from seismic anisotropy. *Nature*, *415*(6873), 777–780. https://doi.org/10.1038/415777a